Bulletin of the Seismological Society of America, Vol. 73, No. 4, pp. 1203–1224, August 1983

GEODETIC MEASUREMENTS OF POSTSEISMIC CRUSTAL DEFORMATION FOLLOWING THE 1979 IMPERIAL VALLEY EARTHQUAKE, CALIFORNIA

BY J. LANGBEIN, A. MCGARR, M. J. S. JOHNSTON, AND P. W. HARSH

ABSTRACT

A geodetic trilateration network comprising 54 baselines was established around the northern part of the Imperial fault beginning 12 days after the Imperial Valley earthquake of 15 October 1979, and the line lengths were repeatedly observed during the following 110 days. During the observational period, there was an average of about 10 cm of dextral postseismic fault slip. Geodetic data in conjunction with alignment-array measurements indicate that the postseismic slip U at time t following the main shock is well described by $U(t) = (10.96 \pm 0.12)$ cm $\log(t/1.75 \text{ days} + 1)$, a result that implies that it will be approximately 9 to 10 yr before the rate of postseismic displacement diminishes to the ambient rate of creep of 0.5 cm/a. The postseismic strain changes are localized to the east side of the Imperial fault in the southern part of the Mesquite Lake basin, where significant north-south extension occurred at an average rate of $2.7 \pm 0.3 \times 10^{-5}$/a during the observational period. These changes are compatible with dextral fault slip within the top 5 km of the fault.

INTRODUCTION

This paper reports the results of repeated trilateration surveys in a region centered about the northern part of the Imperial fault following the Imperial Valley earthquake of 15 October 1979 ($M = 6.6$). Our program of line length measurements was motivated by reports of postseismic fault motion of as much as 10 mm/day (Harsh, 1982) and commenced on 27 October, 12 days after the main shock. The 54 baselines of the network, typically 1 to 2 km long, were measured 6 to 8 times from late October 1979 to mid-February 1980 with a Hewlett Packard 3800A electronic distance-measuring instrument. These data were then analyzed to deduce the fault slip and strain accumulation as functions of position and time.

A preliminary analysis of the data obtained during 1979 was presented by Langbein *et al.* (1982), who interpreted the data in terms of a model of uniform slip over a semi-infinite plane with homogeneous strain changes in the surrounding regions. This report analyzes data extending to mid-February 1980 on the basis of slip across finite fault segments and strain changes in the adjacent regions that vary with time. The extended geodetic data, augmented by results from other studies, allows a more precise description of the postseismic slip as a function of time and position on the fault than in the previous study.

As seen in Figure 1, our geodetic network extends to the northwest of the comprehensive network established in 1970 by the Imperial College of London (Mason *et al.*, 1979). The two networks have three monuments in common, J33, G33, and G34. The new network also includes six alignment-array monuments, HSE1, HSE3, HSW1, HSW3, HSW3′, and HSW4 (Figure 1) installed near the point where the Imperial fault crosses Harris Road (Harsh, 1982). To save time in establishing the network, we used masonry nails driven into the pavement as monuments rather than more stable and permanent marks, such as those employed by Mason *et al.* (1979).

For a number of reasons, the northern part of the Imperial fault is of particular interest with regard to measuring crustal deformation. First, the aftershocks tended to cluster in this region (Johnson and Hutton, 1982; Boore and Fletcher, 1982). Second, the ground rupture was visible and thoroughly documented by Sharp *et al.* (1982). Furthermore, fault afterslip measured using alignment arrays (Harsh, 1982), creepmeters (Cohn *et al.*, 1982), and a small leveling network (Sharp and Lienkaem-

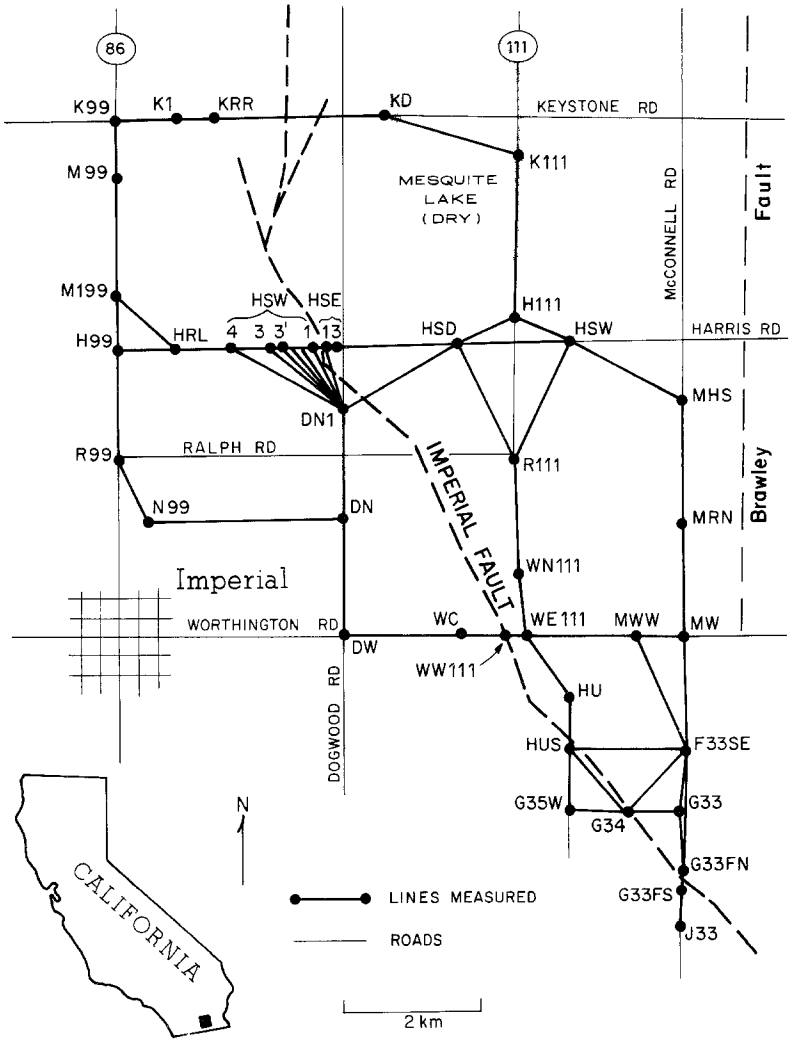

FIG. 1. Locations of the baselines and the northern end of the surface rupture of the 15 October 1979 Imperial Valley earthquake.

per, 1982) is especially well studied in this region. Comprehensive monitoring of crustal deformation in the central and southern parts of the Imperial fault has been reported by Crook *et al.* (1982).

Although postseismic deformation has been measured for a number of previous shocks, most notably the 1966 Parkfield-Cholame earthquake (Smith and Wyss, 1968), a new feature of this study of postseismic ground deformation involves the capability of resolving both strain changes near the fault as a function of time and position and the details of postseismic fault slip. The most novel result of our

observations was evidence for an extensional strain change in the north-south direction on the east side of the northern terminus of the Imperial fault (Figure 1). During the 110-day period of observations, the average rate of change of this strain component was 2.71×10^{-5}/a, a rate which is about two orders of magnitude higher than rates typically measured in southern California (e.g., Savage *et al.*, 1981).

Another result of considerable interest derives from the measurement of postseismic slip estimated using data both from geodetic baselines that cross the fault and alignment arrays (Harsh, 1982). The most comprehensive data set was obtained along Worthington Road (Figure 1) where the combination of the geodetic and alignment data indicate that afterslip is best described by a logarithmic function of time. The derived function is surprisingly consistent with a corresponding result for the 1966 Parkfield-Cholame earthquake (Smith and Wyss, 1968). We found that an inexpensive electronic measuring instrument can be used quite effectively to measure postseismic deformation following some medium-sized earthquakes.

Line-Length Data

The primary data of this study consist of repeated distance measurements (Table 1) over the 54 baselines. Examples of some of the line-length changes are shown in Figure 2. The measurements were made during four periods, late October to early November 1979, mid-November, mid-December, and mid-February 1980; most of the lines were surveyed twice in the first and last periods. The data obtained through mid-December were presented in a preliminary report by Langbein *et al.* (1982).

The electronic distance measuring instrument has a maximum range of about 3 km in ideal conditions and a precision of 3 to 4 mm if corrections are made for pressure, temperature, and relative humidity as measured at both ends of a baseline (Bomford, 1971; Lisowski and Prescott, 1981). Even with an array of 18 corner-cube reflectors, our maximum range in the Imperial Valley was 2.7 km due to the flat topography and high levels of scintillation. Because of the limited range, cross-bracing of quadrilaterals could not always be achieved and so network adjustments (e.g., Bomford, 1971) were not possible.

Surveys of 11 of the 12 lines that span the Imperial fault indicated postseismic displacements far above the expected 4-mm precision of the instrument (Figure 2a); the exception is the northernmost line KD-KRR (Figure 1), which is nearly at right angles to the strike of the fault and where the fault slip (Sharp *et al.*, 1982) was nearly undetectable. All of the fault crossing lines are consistent with postseismic right-lateral fault slip at a rate that diminishes with time.

Of the survey lines that do not cross the fault, some show significant changes in length and others do not, as seen from a sample of 6 of the 43 baselines in Figure 2b. Lines MW-MRN, F33SE-MW, and R111-HSW show about 1 to 2 cm of change, whereas the other three lines do not show appreciable displacements. The results of the strain analysis to follow indicate that most of the line-length changes of significance are localized in the northeast part of the network.

The network was surveyed twice in February 1980, partly to estimate independently the level of precision in our measurement program. As the two surveys were made within 3 days, and because the rate of postseismic deformation at that time was low, the only source of inconsistency between the surveys is presumably measurement error. The rms difference of observed line lengths between these two surveys can be used to estimate the measurement precision, which was found to be 3.1 mm. This estimate of error includes most known sources of potential error including corrections for the index of refraction, short-term oscillator drift, and

TABLE 1

CORRECTED DISTANCES FROM EACH BASELINE WITH DAY 1 CORRESPONDING TO 28 OCTOBER 1979

Baseline	Day No.	Distance (m)	Baseline	Day No.	Distance (m)	Baseline	Day No.	Distance (m)
J33-G33SE		891.000	HUS-G35W		825.000	MWW-F33SE		1649.000
	1	.536		8	0.293		4	0.794*
	6	0.538		17	0.295*		6	0.792
	8	0.540		46	0.291		8	0.799
	17	0.531		107	0.2925		18	0.793*
	46	0.530		108	0.2913		47	0.800
	107	0.5250					107	0.8114
	108	0.5281					108	0.8031
G33FN-G33		618.000	HUS-G34		1178.000	WE111-MWW		1953.000
	8	0.220		8	0.266		4	0.802*
	17	0.212		17	0.267		6	0.793
	46	0.225*		46	0.263		17	0.790*
	48	0.212		108	0.270		47	0.790
				108	0.2659		107	0.7908
							109	0.7878*
F33SE-G33		802.000	WE111-HU		1062.000	WC-WW111		535.000
	8	0.657		8	0.712		4	0.975
	17	0.658		17	0.699		6	0.981
	46	0.653		19	0.702		7	0.977
				46	0.704		18	0.983
				107	0.7100		19	0.982
				109	0.7058		47	0.985
							108	0.9852
							109	0.9894
G35W-G34		804.000	F33SE-MW		1449.00	DW-WC		1621.000
	8	0.434		1	0.338		2	0.257
	17	0.433		6	0.346		4	0.265
	46	0.437		8	0.343		6	0.257
	107	0.4378		17	0.345		7	0.261
	108	0.4384		47	0.349		18	0.260
				107	0.3493		47	0.256
				108	0.3496		108	0.2568
							109	0.2503

DW-DN		1605.000
	2	0.370
	6	0.368
	18	0.370
	47	0.371
	108	0.3705
	109	0.3697
DN-DN1		1776.000
	2	0.971
	5	0.975
	7	0.972*
	17	0.980*
	47	0.977*
	108	0.9755*
	109	0.9735
MW-MRN		1800.000
	1	0.053
	2	0.049
	6	0.057*
	8	0.048*
	18	00.053
	48	00.054
	107	00.0618
	109	00.0635
MRN-MHS		1188.000
	1	0.987
	6	0.998
	8	0.994
	18	0.990
	48	0.996
	107	0.9982
	109	0.9972
HSW-MHS		2013.000
	1	0.273
	6	0.273
	18	0.263
	19	0.269
	109	0.2718
	109	0.2672
HSD-HSW		1607.000
	1	0.849
	5	0.856
	6	0.855
	8	0.853
	18	0.854
	47	0.852
	107	0.8572
R111-HSW		1825.000
	4	0.466
	6	0.468*
	8	0.473
	18	0.471
	48	0.475*
	107	0.4825*
	109	0.4807
HSD-R111		1786.000
	4	0.138
	6	0.136*
	17	0.140*
	47	0.125*
	48	0.153*
	107	0.1521
	109	0.1547
HSD-H111		833.000
	4	0.236
	7	0.240
	18	0.246*
	19	0.239
	47	0.236
	108	0.2369
	109	0.2406
H111-HSW		912.000
	4	0.944
	7	0.948
	18	0.942
	19	0.938
	47	0.941
	108	0.9474
	109	0.9484
HSE3-HSD		1888.000
	1	0.146
	2	0.153
	5	0.146
	7	0.146
	17	0.147
	48	0.154
	107	0.1576
	109	0.1509
WN111-R111		1587.000
	4	0.465
	6	0.464
	18	0.464
	48	0.476
	107	0.4823
	109	0.4831

TABLE 1—*Continued*

Baseline	Day No.	Distance (m)	Baseline	Day No.	Distance (m)	Baseline	Day No.	Distance (m)
WN111-WE111		833.000	K99-K1		991.000	R99-H99		1611.000
	4	0.793		5	0.267		2	0.589
	7	0.789		7	0.264		7	0.596
	17	0.792		18	0.264		18	0.598
	47	0.790		47	0.265		47	0.597
	107	0.7948		108	0.2666		108	0.5921
	109	0.7977		109	0.2688		109	0.6024
H111-K111		2268.000	M99-K99		1374.000	R99-N99		942.000
	4	0.208		5	0.046		2	0.430
	7	0.213*		7	0.044		8	0.437
	18	0.197		18	0.041		18	0.429
	19	0.207*		47	0.044		19	0.435
	47	0.215		108	0.0467		48	0.428
	107	0.2106		109	0.0487		108	0.4334
	109	0.2100*						
KD-K111		1923.000	M199-M99		1045.000	N99-DN		2705.000
	5	0.071		5	0.844		2	0.292*
	7	0.069		7	0.841		8	0.287*
	18	0.063		18	0.836		18	0.271*
	19	0.067*		108	0.846		19	0.261*
	47	0.065		109	0.8448		47	0.271*
	107	0.0660			0.8413		108	0.2809*
	109	0.0725*						
K1-KRRR		565.000	H99-M199		787.000	H99-HRL		851.000
	5	0.531		5	0.973		2	0.839
	7	0.532		7	0.971		7	0.840
	18	0.530		18	0.959		18	0.836
	47	0.527		19	0.976		47	0.833
	109	0.5385		47	0.975		108	0.8376
	109	0.5404		108	0.9744		109	0.8384
				109	0.9742			

M199-HRL		1166.000
	5	0.819
	7	0.819
	18	0.817
	47	0.820
	108	0.8191
	109	0.8183
HRL-HSW4		1555.000
	2	0.003
	5	0.006
	7	0.002
	18	−0.000
	47	−0.001
	108	−0.0058
	109	−0.0060
HSW4-DN1		1034.000
	2	0.297
	5	0.289
	7	0.293
	17	0.289
	48	0.291
	108	0.2851
	109	0.2877
HSW3-DN1		
	7	748.000
	17	0.974
	48	0.972
	108	0.962
	109	0.9679
		0.9761
		746.000
	2	0.459
	7	0.455
	17	0.455
	48	0.457
	108	0.4447
	109	0.4540
HSW1-DN1		727.000
	5	0.376
	7	0.359
	17	0.348
G33FS-G33FN		101.000
	1	0.031
	6	0.024
	8	0.019
	17	0.013
	46	−0.018
	107	−0.0312
	108	−0.0358
	110	−0.0328
G33FS-F33SE		1530.000
	1	0.721
	6	0.710
	8	0.703
	17	0.6925
	46	0.669
	107	0.6436
	108	0.6427
	110	0.6463
G34-G33		796.000
	8	0.125
	17	0.131*
	46	0.138
	48	0.148
G34-F33SE		1191.000
	8	0.081
	17	0.080*
	47	0.069
	107	0.0599
	108	0.0556
HUS-F33SE		1633.000
	8	0.395
	17	0.320*
	46	0.321
	107	0.3670
	108	0.3623
HU-HUS		780.000
	8	0.325
	17	0.309
	46	0.287
	107	0.2704
	108	0.2640

TABLE 1—*Continued*

Baseline	Day No.	Distance (m)	Baseline	Day No.	Distance (m)	Baseline	Day No.	Distance (m)
WW111-WE111		375.000	HSW4-HSD		2421.000			
	4	0.220		2	0.817*			
	6	0.223		5	0.831			
	7	0.225		7	0.823			
	17	0.233		17	0.828*			
	47	0.241		48	0.849			
	107	0.2577		107	0.8603			
	109	0.2587		109	0.8478			
DN1-HSD		1443.000	KRR-KD		2213.000			
	2	0.448		5	0.451*			
	5	0.451		7	0.452			
	7	0.464		18	0.441			
	17	0.465		19	0.443*			
	48	0.469		47	0.449*			
	107	0.4700		108	0.4457*			
	109	0.4728		109	0.4425*			
HSE1-DN1		720.000						
	5	0.606						
	7	0.605						
	17	0.588						
HSW3-HSD		1988.000						
	1	0.092*						
	2	0.122						
	17	0.132						
	48	0.150						
	107	0.1633						
	109	0.1580						

* Poor data quality due to poor seeing conditions.

monument reoccupation. Our error estimate of 3.1 mm is less than the precision of 4.6 mm obtained by Lisowski and Prescott (1981) on a larger set of data. Our higher precision is perhaps partly due to the homogeneous meteorological conditions along the optical path that are associated with the flat terrain. In the analyses to follow, we use 3.8 mm as the estimate of the measurement precision because it is the average of our estimate and that of Lisowski and Prescott.

Postseismic Slip Time History

Postseismic deformation has been found to increase logarithmically with time following the main shock both for earthquakes (Smith and Wyss, 1968) and for mine tremors (McGarr and Green, 1978). Displacements measured over several of the

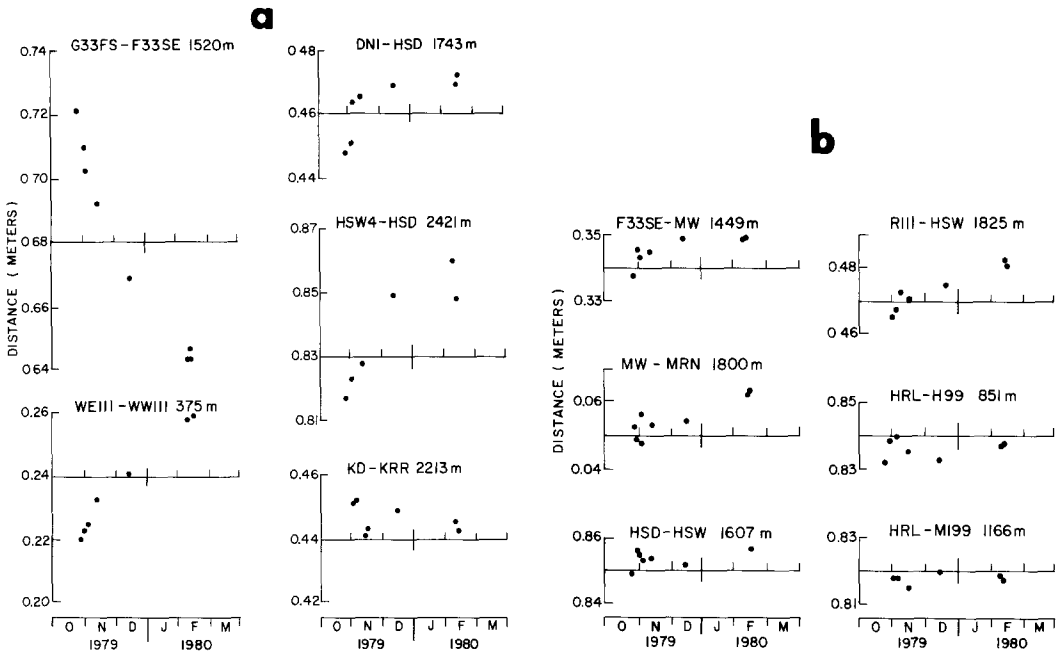

FIG. 2. Representative examples of the change in line lengths from 12 of the 54 measured baselines from the geodetic network in Figure 1. The data in (a) are from baselines that span the Imperial fault; data in (b) are from baselines that do not cross any known faults. Three of the baselines (F33SE-MW, MW-MRN, and R111-HSW) indicate substantial north-south extension on the south shore of Mesquite Lake.

fault-crossing baselines are well suited to establishing the precise time history of postseismic movement because displacement greatly exceeded measurement uncertainty. The data that proved most useful for this purpose were those along Worthington Road WE111-WW111, as fault-slip measurements were made using alignment arrays are also available there (Harsh, 1982).

Accordingly, the geodetic and alignment-array data were used to determine the unknown coefficients in the function describing the postseismic fault slip $U(t)$

$$U(t) = A \log(t/\tau + 1) \tag{1}$$

where time t is defined to be zero at the time of the main shock and where the coefficients A and τ are determined using a least-squares procedure that minimizes the misfit of equation (1) to the observations.

The alignment and geodetic array observations can each be related to the dextral fault slip according to

$$D_a(t) = U(t) + B_a$$
$$= A \log(t/\tau + 1) + B_a \quad (2a)$$

and

$$D_g(t) = U(t)\cos\phi + B_g$$
$$= A \cos\phi \log(t/\tau + 1) + B_g \quad (2b)$$

where $D_a(t)$ is the fault slip measured using the alignment array and $D_g(t)$ represents the line-length changes (in millimeters) observed in this study; ϕ the angle between the geodetic line and the fault strike, is 66° in the case of the WE111-WW111 line.

The unknown constants A, B_a, and B_g in equations (2a) and (2b) were simultaneously determined for various choices of τ using a standard least-squares procedure, and the best choice of τ was taken to be that with the minimum misfit between data and the logarithmic function. The results of this analysis for the Worthington Road

TABLE 2

LEAST-SQUARE FITS OF EQUATION (3) TO OBSERVATIONS ALONG WORTHINGTON ROAD

τ (days)	Misfit (mm/mm)	A (mm)	B_g (mm)	B_a (mm)
4.0	2.16	124.1 ± 2.7	−15.7 ± 2.7	−27.1 ± 2.7
3.0	1.57	118.0 ± 1.8	−18.5 ± 2.0	−34.0 ± 1.5
2.0	1.11	111.3 ± 1.2	−22.7 ± 1.4	−44.6 ± 1.1
1.75	1.08	109.6 ± 1.2	−24.2 ± 1.4	−48.2 ± 1.1
1.5	1.11	107.8 ± 1.2	−26.0 ± 1.4	−52.8 ± 1.2
1.0	1.35	104.0 ± 1.4	−30.9 ± 1.8	−65.2 ± 1.7
0.5	1.83	100.0 ± 1.8	−40.3 ± 2.5	−88.4 ± 2.6

fault crossing are summarized in Table 2, where we see that $\tau = 1.75$ days provides the optimum fit.

The resulting best fit to dextral postseismic slip where Worthington Road crosses the Imperial fault is given by

$$U(t) = (109.6 \pm 1.2)\text{mm} \log(t/1.75 \text{ days} + 1). \quad (3)$$

The fit of equation (3) to the geodetic and alignment-array observations is indicated in Figure 3, along with observations of postseismic creep made along Worthington Road by measuring displacements across a 28-m line of seven steel studs ("nail file") across the fault (Cohn *et al.*, 1982).

It is of interest to compare equation (3) with the results of measuring postseismic vertical displacement where Harris Road crosses the fault. According to Sharp and Lienkaemper (1982), the vertical component of afterslip was given by $V(t) = 86.2$ mm $\log(t/0.95$ days $+ 1)$ where, as before, it is assumed that $V(0) = 0$. The function fit to the vertical afterslip at Harris Road is similar to equation (3) for the dextral slip at Worthington Road.

We also fit the logarithmic functions to our remaining displacement data. Although the logarithmic functions provided a significantly better fit to the fault-

crossing baseline data than linear functions, for the baselines that do not span the Imperial fault, the two functions appear equally adequate.

Changes in Horizontal Strain

Because significant changes in length were measured over many of the lines that did not cross the Imperial fault (Figure 2b), it is clear that observable postseismic strain changes occurred over at least part of our network. To define the pattern of these changes, the geodetic observations are analyzed in terms of several models involving strain as well as fault slip. The inclusion of the more recent data and an areal division of the data differing from that of Langbein *et al.* (1982) yielded the approximate pattern of inhomogeneous strain changes.

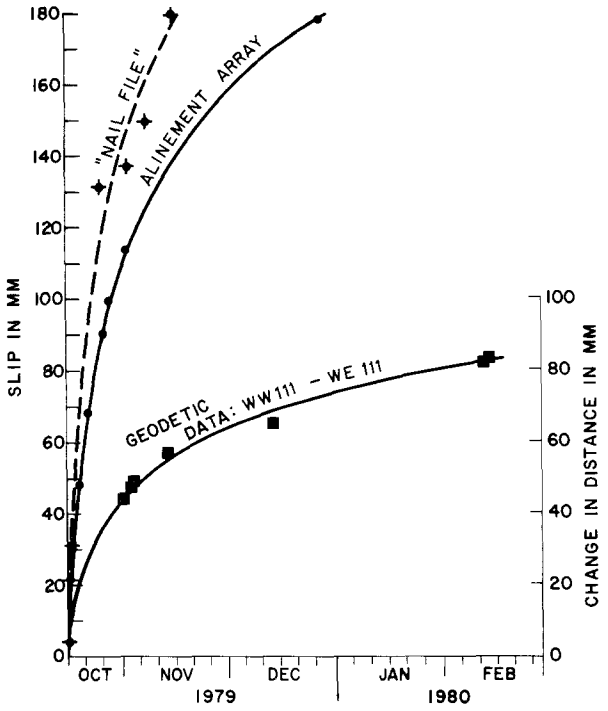

FIG. 3. The observed displacement following the 15 October 1979 earthquake at the Worthington Road fault crossing to the Imperial fault for the 375-m baseline WWIII-WEIII (squares), the alignment array (Harsh, 1982) (circles), and "nail file" array (Cohn *et al.*, 1982) (crosses). Solid lines show the predicted displacements of the geodetic data and alignment array using equation (3). Dashed line shows predicted displacement of the "nail file" if it is assumed to be 1.75 days but where A in equations (2a) and (2b) is 139.2 mm.

The simplest model assumes homogeneous strain accumulation and constant slip over a semi-infinite perfectly planar fault that intersects the surface on the trace of the Imperial fault (Figure 1). For this model, as well as the others to be considered, a line length D_{ij} measured at time t_i over the jth baseline is related to the inferred values of slip U^k and strain $\epsilon_j{}^k$ at time T^k by

$$D_{ij} = D_{0j} + \cos\phi_j\left[U^k\left(\frac{T^{k+1} - t_i}{T^{k+1} - T^k}\right) + U^{k+1}\left(\frac{t_i - T^k}{T^{k+1} - T^k}\right)\right] + D_{ej}\left[\epsilon_j{}^k\left(\frac{T^{k+1} - t_i}{T^{k+1} - T^k}\right) + \epsilon^{k+1}\left(\frac{t_i - T^k}{T^{k+1} - T^k}\right)\right] \quad (4)$$

where $\epsilon_j{}^k = \epsilon_{ee}^k \cos^2 \theta_j + 2\epsilon_{en}^k \cos \theta_j \sin \theta_j + \epsilon_{nn}^k \sin^2 \theta_j$, e and n denote east and north, ϕ_j is the angle between the fault strike and the baseline j, θ_j is the angle between the direction east and baseline j, D_{0j} is the adjusted baseline length, and D_{ej} is the approximate baseline length. As written, this system of equations does not have a unique solution, as is seen most easily by setting $t_i = 0$ and $T^0 = 0$. Then

$$D_{ij} = D_{ej} + U^0 \cos \phi_j + D_{ej}\epsilon^0 j.$$

For each value of j, there is one equation and five unknowns: D_{0j}, U^0, and the three components of $\epsilon_j{}^0$; ϵ_{ee}^0, ϵ_{nn}^0, and ϵ_{en}^0. In general, one finds that there are four more unknowns than equations, and so to solve the equations the slip and strain are assumed to be zero at a specified time, arbitrarily chosen here to occur in January 1980 (Figure 4).

The results of solving equation (4) to deduce relative strains and slip for the approximate epochs of the surveys are shown in Figure 4a, in which time t is measured from the first day of the survey, 12 days after the main shock. In this presentation, the strains have been rotated into a coordinate system for which one of the axes (N45°W) coincides with the approximate strike of the Imperial fault.

The average slip throughout the network inferred for the 110-day period of observations is about 100 mm. For comparison, equation (3), which represents the slip at Worthington Road, yields a slip of 105 mm over this same period. Thus, the postseismic slip at Worthington Road appears to be typical of that along the northern part of the Imperial fault. We also note that a logarithmic function fit to the slip during the five epochs is more satisfactory than a linear function of time.

The three components of strain (Figure 4a) indicate contraction perpendicular to the fault, extension parallel to the fault, and left-lateral shear-strain accumulation. This last component of strain change is consistent with the measured dextral sense of postseismic slip in that fault slip is expected to cause a corresponding strain relaxation on either side of the fault.

The strain changes during the first 10 days of the observational program were particularly rapid and, for the perpendicular and parallel components, were in the reverse sense relative to the overall trend (Figure 4a). The average rates of strain change, fit to the strains in Figure 4a using a least-squares procedure, indicate that the strain component normal to the fault strike contracted at a rate of 18.9 ± 6.0 μstrain/a, the parallel component expanded by 17.0 ± 6.0 μstrain/a, and the sinistral shear component increased at 4.7 ± 2.5 μstrain/a. The corresponding principal strain rates, listed in Table 3, indicate pure or simple shear with the axis of maximum extension nearly parallel to the Imperial fault.

To assess the inhomogeneity of the postseismic strain accumulation, we used equation (4) to infer the strain changes within three regions within the network. The first region includes all of the monuments to the west of the Imperial fault (Figure 1), where Figure 4b and Table 3 show that none of the strain changes are significant at the level of two standard deviations. Part of the reason for the relatively large standard deviations may be the scarcity of diagonal lines in the northwest or northeast directions. In any case, strain changes to the west of the fault appear to be too small to be resolved adequately.

In contrast, the postseismic strain changes on the east side of the fault are substantial (Figure 4c and Table 3). By far the most significant component is north-south extension at a rate of about 20.5 ± 2.7 μstrain/a. An important difference between the strain changes on the east side and those for the entire network is the

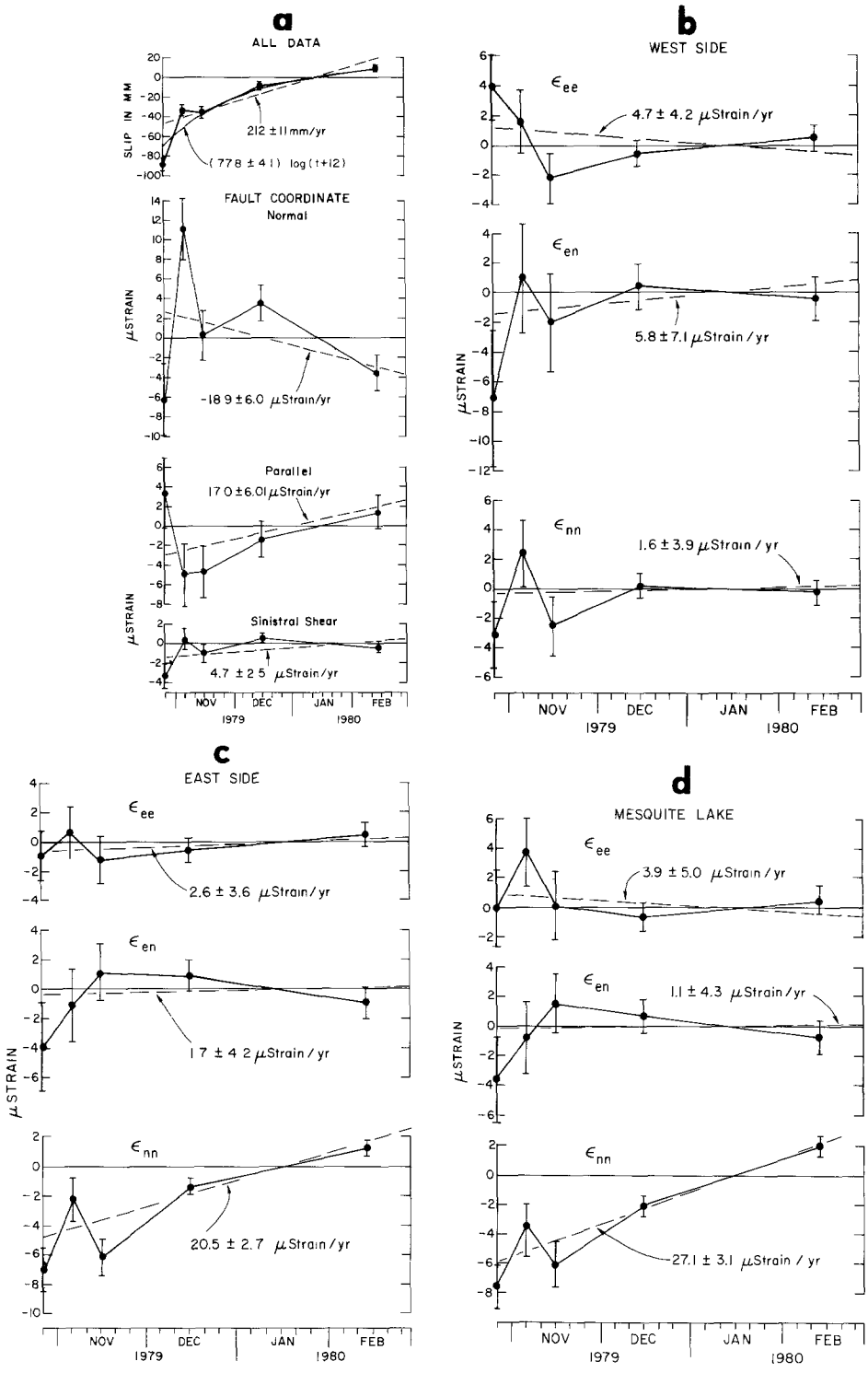

FIG. 4. Plots of the components of the strain tensor and average slip on the Imperial fault for different regions within the geodetic network of Figure 1 starting 12 days after 15 October 1979. (a) Shows slip and strain computed from the data from the entire network. The strain components are rotated to coincide with the strike of the Imperial fault, N45°W. The secular rates of slip and strain as well as the logarithmic function of slip are superimposed on the determination of slip and strain for the time of each survey. (b) to (d) Show the strain changes for the west and east sides of the network and the Mesquite Lake area, respectively. The strain components are oriented on a north-south, east-west coordinate system.

large component of dilatation to the east of the fault of about 23.1 μstrain/a compared to an insignificant dilatational component for either the entire network or the lines to the west of the fault.

An examination of the data indicated that north-south baselines to the east of the fault, between bench mark F33SE and station H111, showed consistent extension, a finding that suggested that much of the north-south extensional strain change was probably concentrated in this region, which is situated on the south slope of Mesquite Lake (dry). As seen in Figure 4d and Table 3, the rate of postseismic north-south extension is impressively large at about 27.1 ± 3.1 μstrain/a with no significant changes in the other components. The rate of dilatation of 23.3 μstrain/a in Mesquite Lake is correspondingly large.

The substantial rate of north-south extension on the southern part of Mesquite Lake is broadly consistent with the tectonics of this area in that this dry lake is at the center of a zone of extension between the northern and southern ends of the Imperial and Brawley faults, respectively (e.g., Weaver and Hill, 1978/1979; Segall and Pollard, 1980). In more detail, however, the north-south extensional direction inferred here for the postseismic deformation is not consistent with extension in the

TABLE 3

PRINCIPAL COMPONENTS OF STRAIN RATE

Subset	Observation No.	No. of Degrees of Freedom	Slip (mm)	Principal Strains (μstrain/yr)		Azimuth of Misfit	
				ϵ_1	ϵ_2	"1" Axis	mm/mm
All data	335	227	77.8 ± 4.1	−20.2 ± 6.0	18.3 ± 6.0	N51.7E ± 4.2°	1.75
Western side	140	114	—	−8.1 ± 7.0	5.0 ± 7.0	N50.3W ± 18.5°	1.16
Eastern side	123	101	—	2.4 ± 3.6	20.7 ± 2.8	N84.5W ± 13.0°	1.07
Mesquite Lake	94	77	—	−3.9 ± 5.0	27.2 ± 3.1	N87.3W ± 10.7°	0.98

east-west direction expected on the basis of the mechanical interaction between the end regions of right-stepping dextral faults (e.g., Segall and Pollard, 1980; Hill, 1982).

Finally, we note that the rather large misfit of 1.75 listed in Table 2 for the entire network is probably associated with the unrealistic assumption of homogeneous strain. The misfit diminished to acceptably low levels near unity after division into subregions indicating that the deduced strains within the smaller area are correspondingly more credible than those for the whole network. If so, then the only postseismic strain change of genuine significance was the north-south extension in Mesquite Lake.

FAULT SLIP AT DEPTH

We attempt here to determine the spatial distribution of fault slip at depth for the period covered in this study by modeling the geodetic data using a least-squares technique. Such analyses generally are difficult because the ability to resolve slip by inverting geodetic data deteriorates rapidly with increasing depth (e.g., Weertman, 1965; Parker, 1977). Statistical significance tests, however, can be used to determine the simplest distribution of slip that is consistent with the data.

For modeling purposes, the Imperial and Brawley faults were divided into a series of linked, planar, vertical faults that coincide with the surface traces. The substantial variation in strike of the Imperial fault over its northern part suggested division into

seven segments (Figure 5) whereas the Brawley fault could be adequately approximated with two segments, with the division point located 1.8 km north of Worthington Road (even with station MRN). The geodetic network did not span the Brawley fault (Figure 1), and the amount of slip of this fault is difficult to resolve with any certainty.

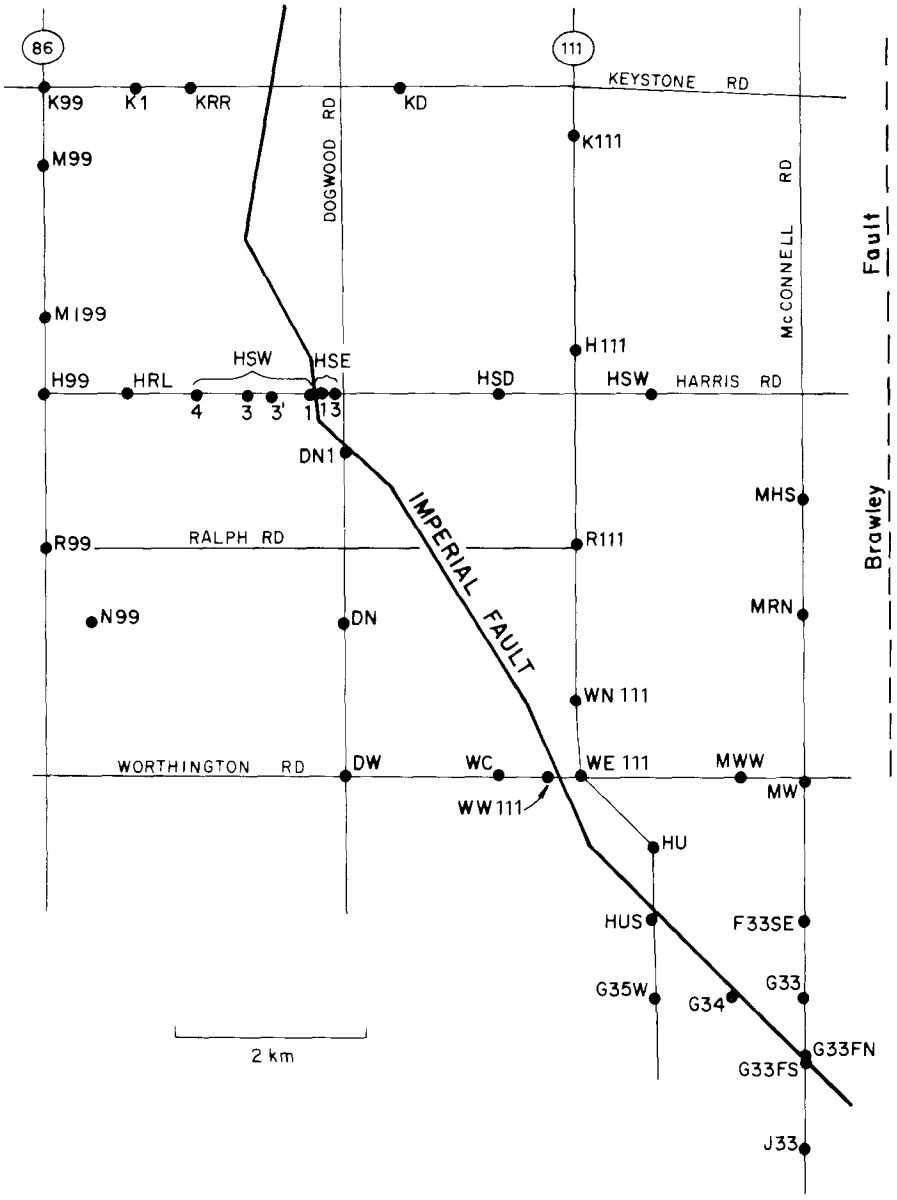

FIG. 5. The trace of modeled Imperial and Brawley faults used for determining the slip at depth. Locations of bench marks are also shown.

In addition to the horizontal segmentation, the fault planes were arbitrarily divided vertically into two zones. The top zone extends from the surface to 750 m depth, and the bottom zone extends to a depth determined from the observations. This depth is defined such that slip below cannot be resolved with any confidence from the data.

Because vertical as well as horizontal postseismic displacement was observed (Sharp *et al.*, 1982; Sharp and Lienkaemper, 1982), it was necessary to assume both types of slip on each of the fault elements. Thus, the initial model comprised 14 fault elements for the Imperial and 4 for the Brawley for a total of 18 elements. Thus, with two components of slip per element, there were 36 unknowns to be determined from the geodetic observations.

Data for some of the 54 baselines seemed inappropriate for modeling fault slip at depth because a number of the monuments were suspected of being within the fault zone. Thus, observations for baselines involving G33FS, G33FN, HUS, WW111, DN1, and HSE3 were not considered. In addition, bench mark G33 was destroyed sometime between the surveys in December 1979 and February 1980, rendering the data from these baselines useless for the present purpose. After these reductions in the data set, observations over 31 baselines remained from which to determine the 36 unknown components of fault slip.

For the purpose of determining fault slip, the total change in length over each baseline was approximated by a linear or logarithmic function of time using a least-squares procedure. Hence, the total displacements determined by the rates of length change for the 110-day period for each of the 31 baselines used here make up the data set used to solve for the unknown components of slip. Initially, as there were 31 equations and 36 unknowns, we neglected the possibility of slip on the Brawley fault, thereby reducing the number of unknowns to 28.

The next step in the inversion procedure was to use the F test as a rationale for removing partitions between adjacent fault elements so as to reduce the number of unknowns. The F test allows the variance of the misfits of two models to be compared using the ratio

$$F = \frac{[(d - Au)^t(d - Au) - (d - A'u')^t(d - A'u')]/(f_1 - f_2)}{[(d - Au)^t(d - Au)]/f_1}$$

which is Fisher distributed and is tabulated (e.g., Brieman, 1973). The quantity $(d - Au)$ represents the difference between observations d and computed displacements Au for model u, and $(d - A'u')$ corresponds to the misfits predicted from model u' for which a partition has been removed, thus reducing the number of unknowns by one. f_1 and f_2 represent the degrees of freedom for models u and u', respectively, and a superscript t indicates the transpose of a matrix.

After employing the F test to determine all the partitions that are not required at the 99 per cent confidence level, the model that resulted, and which had the smallest misfit, is indicated by the solid lines in Figure 6a; the dashed lines show where partitions were removed. It was not necessary to include the Brawley fault in the model because its computed value of slip is not significant at the 90 per cent confidence level. Similarly, slip below a depth of 5 km cannot be resolved at the 90 per cent confidence level and is, therefore, taken to be zero. In the final model, then, the differences in slip components between neighboring fault elements are significant at the 99 per cent confidence level, with the exception of the vertical slip determined for the Keystone Road segment, which is not significant even at the 90 per cent confidence level but is included here for completeness.

The final step in this analysis was to employ the F test to infer the smallest depth D_2 to the bottom of the second layer for which the slip beneath D_2 becomes statistically significant. Because in the present model, slip below 5 km is not significant at the 90 per cent confidence level, several models with smaller values of

D_2 were tested. For D_2 = 3 km, the vertical component of slip at greater depths is significant at the 90 per cent confidence level, and the corresponding value of D_2 for the horizontal slip is 2 km. Thus, from the statistics, slip below D_2 has no significant effect on the data inversion as long as D_2 is 4 km or greater. If D_2 is as shallow as 3 km, then the subadjacent slip should be taken into account.

The model in Figure 6a has a value of 0.81 mm/mm as the rms value of the ratio of the model misfits to the observational error of the data. A misfit of 0.98 mm/mm was obtained if we restricted the vertical offset to be zero south of Dogwood Road, which is consistent with the observations of surface rupture made by Sharp and Lienkaemper (1982). The major difference between this model (Figure 6b) and the

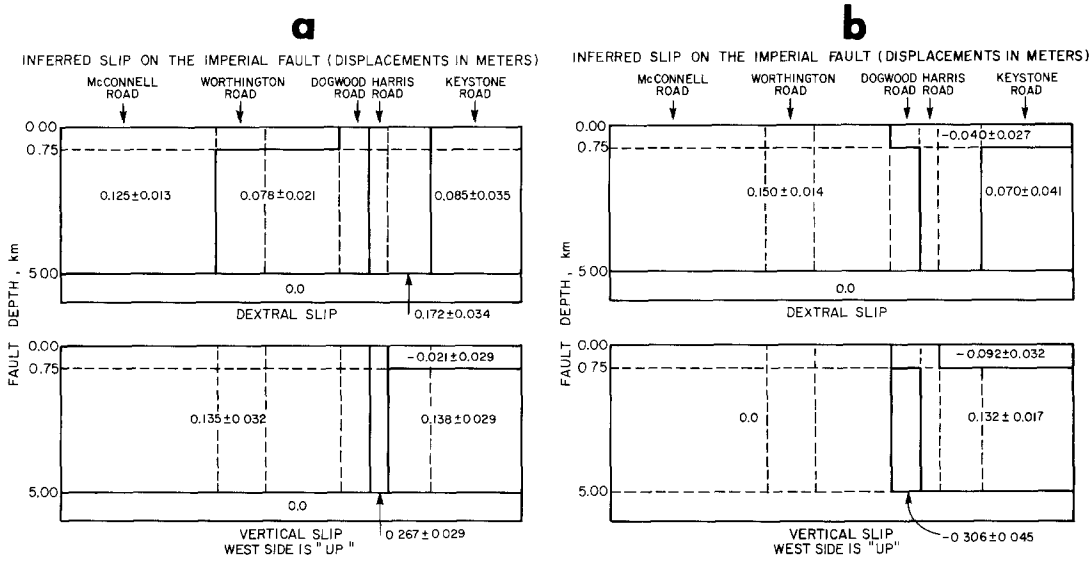

FIG. 6. Profiles of the inferred slip distribution, in meters, on the Imperial fault. Cultural features such as roads are indicated. The dashed lines show the original partitions of the fault. (a) Shows the slip model where both horizontal and vertical slip are allowed on all of the partitions in the fault model. The misfit of this model to the data is 0.81 mm/mm and the vertical component of slip beneath Keystone Road is not significant to the 90 per cent confidence level. Slip on the Brawley fault was found to have the same degree of insignificance and is taken to be zero. In (b), the slip distribution is shown for the Imperial fault where the vertical slip south of Dogwood Road is assumed to be zero. For this model, the data misfit is 0.98 mm/mm, and for the segment of the Brawley fault north of station MRN, 0.044 ± 0.017 meter of dextral slip is inferred. The inferred sinstral slip north of Dogwood Road is not significant to the 90 per cent confidence level, but the dextral slip at depth beneath Keystone Road is significant at the 95 per cent confidence level.

previous model is the inference of significant dextral slip on the Brawley fault and a smaller amount of sinistral slip on the Imperial fault north of Dogwood Road. In fact, the inferred 4 cm of left-lateral slip north of Dogwood Road is not significant at the 90 per cent confidence level. Dextral slip below D_2 becomes significant at the 90 per cent confidecnce level for $D_2 \leqq 3$ km.

LOWER BOUND ON DEPTH OF POSTSEISMIC SLIP

A linear programming technique described by Langbein (1981) can be applied to the geodetic data to estimate the minimum depth to which slip must occur. Essentially, the fault plane is divided into a number of elements vastly exceeding the number of geodetic observations. Next, a linear programming algorithm is used to select the slip distribution that minimizes a specified linear function of slip, i.e.,

the moment, which is proportional to

$$\sum_{i=1}^{M} u_i A_i \tag{5}$$

where the fault has been divided into M elements, with the ith element having slip u_i and area A_i.

Because the postseismic slip diminished markedly with distance north of Harris Road (Sharp *et al.*, 1982), only the part of the network to the south of Ralph Road was used to model a section of the fault for which the slip distribution is assumed to be homogeneous along strike. The baselines best suited to this analysis are DW-DN, DW-WC, WN111-R111, WE111-MWW, F33SE-MW, F33SE-MWW, MW-MRN, and MRN-MHS.

For purposes of the analysis, the vertical fault plane is divided into a series of infinitely long horizontal strips of equal thickness extending to a maximum depth D, taken as 10 km here. The linear programming technique involves determining a distribution of slip U_j such that

$$d_i - \sigma_i \leqq \sum_{j=1}^{M} A_{ij} u_j \leqq d_i + \sigma_i \tag{6}$$

and which minimizes the quantity $D \sum_{j=1}^{M} u_j$, which is equivalent to minimizing the moment. The subscript i refers to the observed change d_i in line length of the ith baseline, the matrix A_{ij} relates the slip on fault strip j to the change d_i in baseline i, and σ_i is a measure of the uncertainty in d_i; in the present application, σ_i is taken as the standard deviation of fitting a linear function of time to the observed length changes over baseline i.

The computational procedure for solving equations (5) and (6) was outlined by Luenberger (1973) and Langbein (1981); the results for various models are listed in Table 4. We modeled four different slip regimes on the Imperial and Brawley faults: (1) dextral and vertical slip on the Imperial fault only; (2) dextral and vertical slip on the Imperial fault and 10 cm of dextral slip on the Brawley; (3) dextral slip on the Imperial fault only; and (4) dextral slip on both faults but allowing only 4 cm of slip on the Brawley fault, which is the amount inferred for the model in Figure 6b. To test whether the models are consistent with the data used in equation (6), the number of strips was varied to verify that the product of slip and depth remained relatively invariant. Invariance was not the case with the two models that restricted the slip on the Imperial fault to be purely right-lateral. The model involving only dextral slip on both faults is compatible with a data set that excludes the baseline DW-DN. The reason for this exclusion is that the data from DW-DN had the second largest misfit of the set of 31 baselines used to infer the slip shown by the model in Figure 6b. Eliminating DW-DN from the data set does not improve the invariance for the model that assumes no slip on the Brawley fault since the product of slip and depth changes by nearly half when the number of strips is quadrupled, which indicates that this simple model of slip is not consistent with the observations.

The most useful quantity listed in Table 4 for the purpose of estimating the minimum depth of postseismic slip is the product of slip and depth. If the fault slip estimated from the fault-crossing baseline and alignment-array measurements (Harsh, 1982) is representative of postseismic slip in the top few kilometers of the fault zone, then from equation (3), the slip occurring between 12 and 122 days after

the main shock is 10.5 cm, which, if divided into the last column of Table 4, yields, in principle, the lower limits on the depth of postseismic slip. For the three models that are consistent with the data, the estimates on the lower bounds range from 800 to 2900 m, which is a clear indication that the models limiting the slip to be at depths less than 800 m are not consistent with the data. If, for instance, we exclude the results based upon allowing only dextral slip on the Imperial fault, since that model has been found to be only marginally consistent with the line-lengthening data, then the lower limit of postseismic slip becomes 1700 or 2900 m with either 10 or 0 cm, respectively, for the assumed value of slip on the Brawley fault. The bound of 2.9 km is in close agreement with the minimum depth of about 3 km necessary for adequately satisfying the observations using the least-squares method and the model involving zero slip on the Brawley fault (Figure 6a). It should be remembered, however, that the linear programming result is also compatible with a smaller lower bound on depth but with correspondingly greater average slip. A solution with a

TABLE 4

THE MINIMUM AVERAGE SLIP COMPUTED FOR DIFFERENT FAULT GEOMETRIES

Allowed Vertical Slip on Imperial Fault	No. of Strips	No. of Unknowns	Assumed Value of Dextral Slip on the Brawley Fault (m)	Imperial Fault	
				Minimum Average Slip in Top 10 km (m)	Minimum Average Slip × 10 km (m^2)
Yes	50	100	0.0	0.0329	328.97
Yes	100	200	0.0	0.0309	309.40
No	100	100	0.04	0.0102	102.17*
No	200	200	0.04	0.0097	97.78*
No	400	400	0.04	0.0085	85.38*
No	100	100	0.0	0.0422	422.25*
No	200	200	0.0	0.0362	361.58*
No	400	400	0.0	0.0204	203.41*
Yes	50	100	0.1	0.0210	209.57
Yes	100	200	0.1	0.0178	178.04

* Excludes DW-DN.

substantially reduced depth, however, would lead to high levels of slip concentrated near the surface so that such a model would be difficult to reconcile with the geodetic observations.

DISCUSSION

It is of interest to compare the postseismic fault slip, as represented by equation (3), with the preseismic and coseismic displacements. According to Cohn *et al.* (1982), creepmeter records along the Imperial fault indicate that creep occurs episodically with events having displacements of about 1 cm happening approximately once every 2 yr. They concluded that the average rate of fault creep is about 0.5 cm/a. This value of secular creep should be used as a lower bound on the creep rate as Lisowski and Prescott (1981) report that creep rate measured by creepmeters is commonly less than the rate determined from geodetic measurements. For comparison, from equation (3), the total postseismic fault slip expected during the first year after the main shock is 25.5 cm or an average rate about 50 times higher than the preseismic rate. Equation (3) also implies that the rate of postseismic slip

will diminish to the preseismic rate after $9\frac{1}{2}$ yr during which time a total of 36 cm of postseismic slip will have accumulated. This finding is in reasonable agreement with a corresponding result by Cohn *et al.* (1982), who analyzed displacements measured across their "nail file" array at the Anderholt Road crossing of the Imperial fault, south of our network, and concluded that the postseismic slip rate would diminish to the preseismic rate after 6 yr.

Equation (3) can be used in conjunction with the "nail file" data of Cohn *et al.* to estimate the coseismic slip at Worthington Road. The displacement measured between the time of the last preearthquake survey of the nail file on 20 August 1981 and the first postseismic survey 8 hr after the main shock was 12.1 cm. From equation (3), the postseismic slip after 8 hr is 0.8 cm. If any preearthquake slip between 20 August and 15 October can be neglected on the basis of the annual rate of 0.5 cm/a then the coseismic displacement is 11.3 cm.

The total predicted postseismic slip of 36 cm exceeds the coseismic slip by more than three times. Furthermore, our estimate of the coseismic displacement of about 11 cm is in reasonable agreement with the results of the strong-ground-motion modeling of Hartzell and Helmberger (1982), who concluded that the fault slip in the upper 5 km was generally quite low, ranging from 0 to about 25 cm; in contrast, their values of coseismic displacements were as high as 250 cm below 5 km.

Our findings regarding postseismic fault slip have some features in common with corresponding results for the 1966 Parkfield, California, earthquake reported by Smith and Wyss (1968). From their postseismic triangulation data at the Taylor Ranch, we inferred that

$$U(t) = 95.4 \log(1 + t/1.47)$$

where t is in days following the main shock, and $U(t)$ is in millimeters. The agreement between this Parkfield time history of postseismic slip and equation (3) is curious, although probably coincidental.

The postseismic strain changes depart substantially from expectations in that the only significant strain accumulation is on the east side of the fault where there is a substantial dilatation. Our expectation, in contrast, is for dilatation on the east side and a comparable amount of contraction on the west side of the northwestern terminus of the fault. The coincidence of the zone of concentrated postseismic strain accumulation with the Mesquite Lake depression is reassuring and it should be noted in this regard that there are no obvious compressional features on the west side of the fault. Nevertheless, we are at a loss to explain why the strain accumulation is detectable only on the east side.

The postseismic strain accumulation in the Mesquite Lake basin was almost exactly opposite in sense to the regional strain change for the period 1972 to latter 1979 determined by Savage *et al.* (1981) for their Salton network, which extends northwestward from the northwestern end of the Imperial fault. During that period the principal strain rates are north-south contraction at a rate of 2.1×10^{-7}/a and east-west extension at 1.4×10^{-7}/a. For comparison, the principal strain change in the southern part of the Mesquite Lake during this study period is a north-south extension at an average rate of 2.71×10^{-5}/a, more than 100 times greater in rate than the long-term regional contraction.

Although our geodetic network was too small to ascertain boundaries on the extent of this remarkably high rate of strain accumulation, its coincidence and localization within the network to the southern part of the Mesquite Lake depression

suggests that the total zone of marked postseismic strain accumulation for the northern part of the Imperial fault is limited to this basin. More specifically, the modeling of fault slip using the least-squares technique indicates that the high rate of north-south extension corresponds to postseismic slip in the upper 5 km of the fault.

The focal mechanisms of the aftershocks near the northern part of the Imperial fault (Boore and Fletcher, 1982) are for the most part consistent with dextral slip on northwest-striking, near-vertical fault planes; these mechanisms are thus generally consistent with that of the main shock. The tension axes tend to be oriented east-west whereas the compression axes vary in direction from north-south to vertical; thus the focal mechanisms indicate east-west extension. This means that the seismic deformation is not consistent with the geodetic results reported here of north-south extension beneath the Mesquite Lake basin. Thus, the aftershocks do not appear to be related to the postseismic strain changes measured in the Mesquite Lake basin.

A resolution of this discrepancy is possible. The geodetic results can be explained in terms of fault slip in the top 5 km or less whereas all but 1 of the 12 aftershocks reported by Boore and Fletcher (1982) were located at depths between 4.2 and 8.0 km. Hence, the north-south extension beneath the Mesquite Lake basin may be a fairly shallow phenomenon confined to the topmost 4 km or so.

Finally, we note a curious aspect of the distribution of fault slip shown in Figure 6. To the north of Harris Road, the fault trace swings to a north-northeasterly orientation (Figures 1 and 5) and yet the sense of slip is nevertheless dextral; field observations by Sharp *et al.* (1982) corroborate this result. Thus, in the vicinity of Keystone Road, the local tectonics involving east-west contraction appears to differ significantly from the regional tectonics for which north-south contraction is the rule. As none of the aftershocks have focal mechanisms appropriate to dextral slip on north-northeast-oriented fault planes (Boore and Fletcher, 1982), it appears likely that this inhomogeneity in the tectonic regime is a fairly shallow (perhaps the top 5 km or less) phenomenon.

Acknowledgment

Mention of specific products is for descriptive purposes only and does not constitute an endorsement by the U.S. Geological Survey.

References

Bomford, G. (1971). *Geodesy*, Oxford University Press, London, England.

Boore, D. M. and J. B. Fletcher (1982). A preliminary study of selected aftershocks from digital acceleration and velocity recordings *U.S. Geol. Surv. Profess. Paper 1254*, The Imperial Valley, California, earthquake of October 15, 1979, 109–118.

Brieman, L. (1973). *Statistics: With a View Toward Applications*, Houghton-Mifflin Company, Boston, Massachusetts.

Cohn, S. N., C. R. Allen, R. Gilman, and N. R. Goulty (1982). Preearthquake and postearthquake creep on the Imperial fault and the Brawley fault zone, *U.S. Geol. Surv. Profess. Paper 1254*, The Imperial Valley, California, earthquake of October 15, 1979, 161–167.

Crook, C., R. G. Mason, and P. R. Wood (1982). Geodetic measurements of horizontal deformation on the Imperial fault, *U.S. Geol. Surv. Profess. Paper 1254*, The Imperial Valley, California, earthquake of October 15, 1979, 183–191.

Harsh, P. W. (1982). Distribution of afterslip along the Imperial fault, *U.S. Geol. Surv. Profess. Paper 1254*, The Imperial Valley, California, earthquake of October 15, 1979, 193–203.

Hartzell, S. H. and D. V. Helmberger (1982). Strong motion modeling of Imperial Valley earthquake of 1979, *Bull. Seism. Soc. Am.* **72**, 571–596.

Hill, D. P. (1982). Contemporary block tectonics: California and Nevada, *J. Geophys. Res.* **87**, 5433–5450.

Johnson, C. E. and L. K. Hutton (1982). Aftershocks and preearthquake seismicity, *U.S. Geol. Surv. Profess. Paper 1254*, The Imperial Valley, California, earthquake of October 15, 1979, 59–76.

Langbein, J. O. (1981). An interpretation of episodic slip on the Calaveras fault near Hollister, California, *J. Geophys. Res.* **86,** 4941–4948.

Langbein, J., M. J. S. Johnston, and A. McGarr (1982). Geodetic observations of postseismic deformation around the northern end of the surface rupture, *U.S. Geol. Surv. Profess. Paper 1254*, The Imperial Valley, California, earthquake of October 15, 1979, 204–211.

Lisowski, M. and W. H. Prescott (1981). Short-range distance measurements along the San Andreas fault system in central California, 1975 to 1979, *Bull. Seism. Soc. Am.* **71,** 1607–1624.

Luenberger, D. G. (1973). *Introduction to Linear and Nonlinar Programming*, Addison-Wesley Publishing Co., Reading, Massachusetts.

Mason, R. G., J. L. Brander, and M. G. Bill (1979). Mekometer measurements in the Imperial Valley, California, *Tectonophysics* **52,** 497–503.

McGarr, A. and R. W. E. Green (1978). Microtremor sequences and tilting in a deep mine, *Bull. Seism. Soc. Am.* **68,** 1679–1697.

Parker, R. L. (1977). Understanding inverse theory, *Ann. Rev. Earth. Planet. Sci.* **5,** 35–64.

Savage, J. C., W. H. Prescott, M. Lisowski, and N. E. King (1981). Strain accumulation in southern California, 1973–1980, *J. Geophys. Res.* **86,** 6991–7001.

Segall, P. and D. D. Pollard (1980). Mechanics of discontinuous faults, *J. Geophys. Res.* **85,** 4337–4350.

Sharp, R. V. and J. J. Lienkaemper (1982). Preearthquake and postearthquake near-field leveling across the Imperial fault and the Brawley fault zone, *U.S. Geol. Surv. Profess. Paper 1254*, The Imperial Valley, California, earthquake of October 15, 1979, 169–181.

Sharp, R. V., *et al.* (1982). Surface faulting in central Imperial Valley, *U.S. Geol. Surv. Profess. Paper 1254*, The Imperial Valley, California, earthquake of October 15, 1979, 119–143.

Smith, S. W. and M. Wyss (1968). Displacement on the San Andreas fault initiated by the 1966 Parkfield earthquake, *Bull. Seism. Soc. Am.* **68,** 1955–1974.

Weaver, C. S. and D. P. Hill (1978/1979). Earthquake swarms and local crustal spreading along major strike slip faults in California, *Pure Appl. Geophys.* **117,** 51–64.

Weertman, J. (1965). Relationship between displacement on a free surface and the stress on a fault, *Bull. Seism. Soc. Am.* **55,** 945–953.

U.S. GEOLOGICAL SURVEY
OFFICE OF EARTHQUAKES, VOLCANOES AND ENGINEERING
345 MIDDLEFIELD ROAD
MENLO PARK, CALIFORNIA 94025

Manuscript received 16 August 1982